RSC Advances

PAPER

View Article Online
View Journal | View Issue

Cite this: *RSC Adv.*, 2025, **15**, 36084

CO_2 adsorption and activation on $AuO(CO_2)_n^{-/+}$ ($n = 1$–3) clusters: a theoretical study

Wei Huang,[a] Wenbao Zhao,[a] Zonghui Guo,[a] Shihu Du,[bc] Jincheng Tian,[a] Ruoying Zhang,[a] Haiyan Han, *[a] Zhi Zhao,*[ac] Wei Pei, [d] Ruili Shi*[a] and Hua Xie *[c]

Received 24th June 2025
Accepted 22nd September 2025

DOI: 10.1039/d5ra04472c

rsc.li/rsc-advances

The geometric and electronic properties of $AuO(CO_2)_n^{-/+}$ ($n = 1$–3) clusters have been systematically investigated using density functional theory (DFT). All anionic ground states are singlets, whereas the cationic counterparts are triplets. Anions prefer distorted CO_3-like binding and, at $n = 3$, an oxygen-bridged ring, while cations retain near-linear CO_2 with modest perturbation. The thermodynamics at 298 K show favorable first and second adsorption on anions and an unfavorable third step, consistent with site saturation. In cations the first step is favorable, the second weakly favorable, and the third slightly unfavorable. Natural population analysis (NPA) and Natural bond orbital (NBO) analyses indicate stronger charge acceptance and higher Au–O bond order in anions than in cations. These results identify charge state and saturation as the primary controls of bonding across this size range.

1 Introduction

Over the past century, the widespread use of fossil fuels has resulted in a notable elevation of carbon dioxide levels in the atmosphere, precipitating a cascade of environmental concerns, including global warming, ocean acidification, and sea level rise.[1–3] A substantial body of research has been dedicated to the storage and fixation of carbon dioxide. Converting CO_2 into value-added chemicals, fuels, or materials would transform it into an abundant and inexpensive carbon source. CO_2 reduction begins with charge transfer, activating the C=O bonds and generating anionic radicals.[4] However, CO_2 is a highly stable molecule with strong bond energy and no dipole moment, making the reduction process challenging. Therefore, a suitable catalyst is essential to lower the activation barrier for CO_2 reduction. A range of approaches have been widely explored for CO_2 reduction, including electrocatalysis, biocatalysis, and photocatalysis.[5–10]

Although CO_2 reduction is crucial for both environmental protection and chemical applications, the intrinsic mechanisms of the reaction remain poorly understood due to the complexity of the environment. Isolated gas-phase clusters with clear structural definition serve as valuable models for studying chemical reactions, enabling comprehensive exploration of molecular structures and activation mechanisms,[11–20] while also providing valuable insights into the mechanistic steps involved in CO_2 activation reactions.

Metal oxides, in particular, have demonstrated substantial catalytic capabilities in various chemical processes, including the activation and reduction of CO_2. Metal oxide materials, such as TiO_2, CuO, and CeO_2, have been extensively used in photocatalytic and electrocatalytic applications due to their unique surface reactivity, stability, and redox properties.[21–23] These metal oxides are known to interact with CO_2, facilitating electron transfer and leading to the formation of carbonate or other intermediates that are crucial for CO_2 conversion into value-added products.[24–26] Infrared photodissociation studies reveal that ScO^+, YO^+, and HoO^+ cations undergo transformation from solvated states to carbonate structures upon binding CO_2, whereas LaO^+ only forms solvated structures.[27–29] Meanwhile, highly oxygenated metal oxides have also gained much attention. Liu *et al.* found that with additional CO_2 coordination, $Sc_2O_2^+$ and $Sc_3O_4^+$ cations can effectively promote the fixation of CO_2 into carbonate groups.[30,31] Reactions of NiO_2^+, NbO_2^+, TaO_2^+, and TaO_3^+ cations with multiple CO_2 molecules have shown no substantial CO_2 activation.[32–35] Through infrared spectroscopy studies on the interaction between $Mn_xO_y^+$ ($x = 2$–5, $y \geq x$) and CO_2, Lang *et al.* revealed that the interaction is primarily electrostatic.[36] Mikolaj *et al.* reported that CO_2 activation on copper oxide anions primarily leads to CO_3 formation.[37]

[a]*School of Mathematics and Physics Science and Engineering, Hebei Computational Optical Imaging and Photoelectric Detection Technology Innovation Center, Hebei International Joint Research Center for Computational Optical Imaging and Intelligent Sensing, Hebei University of Engineering, Handan 056038, China. E-mail: hanhy0226@163.com; zhaozhi@hebeu.edu.cn; shiruili@hebeu.edu.cn*

[b]*School of Chemistry and Chemical Engineering, Shandong University, Jinan 250100, China*

[c]*State Key Laboratory of Molecular Reaction Dynamics, Dalian Institute of Chemical Physics, Chinese Academy of Sciences, Dalian 116023, China. E-mail: xiehua@dicp.ac.cn*

[d]*College of Physics Science and Technology, Yangzhou University, Yangzhou 225009, China*

Meanwhile, there is a notable lack of research focused on the ability of metal oxide anions to induce CO_2 carbonation. Hossain and co-workers observed that $W_xO_y^-$ shows no evidence of dissociative adsorption of CO_2.[38] In $[TiO_x(CO_2)_y]^-$ systems, the study demonstrates a diversity of ligand motifs depending on the oxidation state, with carbonate ligands being the most stable across all oxidation levels, and additional oxalate, η^2-(C,O), η^2-(O,O), and carbonyl ligands observed at lower oxidation states.[39]

In the context of gold-based catalysts, well-defined gas-phase clusters have exhibited distinct adsorption behaviors toward small molecules such as O_2, CO, and N_2, often influenced by cluster size and charge state.[40–42] Molecular oxygen can chemisorb as superoxo or peroxo species depending on the cluster size and the charge state.[40] Molecular nitrogen, in contrast, is typically weakly adsorbed and may only be observed under cryogenic conditions.[42] These adsorption characteristics are underpinned by the unique electronic properties of gold clusters, including relativistic effects and quantum size-dependent behavior, which also play a critical role in their catalytic performance.[43,44] Recent reviews on gold catalysis further emphasize the significant effects of particle size and support interactions, highlighting the importance of interfacial charge transfer and dynamic redox cycles in gold-mediated transformations.[45–47]

Despite these advances, the reactivity of gold oxide clusters toward CO_2 remains underexplored. Although earlier gas-phase studies have characterized anionic AuO *via* photoelectron spectroscopy, reporting the electron affinity of neutral AuO and its spin–orbit splitting,[48] and the electronic structure of cationic AuO has been characterized theoretically,[49] systematic studies on CO_2 adsorption and activation on AuO_n clusters are still lacking.[50] Both cationic and anionic Au_nO_m clusters have demonstrated reactivity toward small molecules, suggesting their potential utility in CO_2 conversion.[51,52] Given the unique electronic properties of gold and its potential to enhance catalytic performance, this work is dedicated to exploring the adsorption and activation of CO_2 on $AuO(CO_2)_n^{-/+}$ (n = 1–3) clusters. By employing advanced quantum chemical methods, we systematically examine the geometric and electronic structures of these clusters, analyze their charge distributions, and elucidate the underlying mechanisms that govern CO_2 activation. The insights gained from this study are expected not only to deepen our fundamental understanding of CO_2 conversion processes in gold-based systems but also to provide valuable guidelines for the rational design of efficient catalysts for CO_2 reduction.

2 Theoretical method

The structural searching program Molclus[53] was employed to generate candidate initial structures for $AuO(CO_2)_n^{-/+}$ (n = 1–3) clusters. Geometry optimizations were performed at the B3LYP-D3 (ref. 54–56)/def2-TZVP[57,58] level of theory. This level is a commonly used, well-balanced choice for Au chemistry. Literature benchmarks on the def2 basis framework and on gold bonding, together with Au-oxide case studies, support its use for Au–X bonding.[57,59,60] To assess functional and basis set sensitivity, key isomers were re-evaluated at five cross-check levels: (i) B3LYP-D3 with the LANL2DZ[61–63] effective core potential for Au and 6-311+G(3df)[64] for C and O; (ii) ωB97X-D[65] with the same LANL2DZ/6-311+G(3df); (iii) M06-2X[66] with LANL2DZ/6-311+G(3df); (iv) ωB97X-D/def2-TZVP; (v) M06-2X/def2-TZVP. The data are summarized in Tables S1 and S2 in the SI. Table S1 shows that the relative energy with zero-point energy correction remains consistent for clusters with $n = 1$ and $n = 3$ across all tested methods. For $n = 2$, some functional dependence in relative energy is observed. Though Table S2 shows that the geometric structures remain largely consistent. Harmonic frequency analysis was conducted at the same level of theory with geometry optimizations to ensure that the optimized structures corresponded to true minima on the potential energy surfaces, with no imaginary frequencies observed. Gibbs free energies at 298 K were obtained from the same frequency calculations to evaluate the thermodynamic favorability of CO_2 adsorption. Different spin multiplicities were evaluated, and the results are summarized in Table 1. The lowest-energy states for $AuO(CO_2)_n^-$ (n = 1–3) corresponds to singlet ground states, while the lowest-energy state for $AuO(CO_2)_n^+$ (n = 1–3) corresponds to triplet ground states. To quantify bonding and activation we carried out single-point Natural Bond Orbital analysis (NBO)[67] and Natural Population Analysis (NPA) on the optimized structures. All calculations were performed using the Gaussian 09 program.[68]

3 Result and analysis

3.1 Structures and relative energies

Fig. 1 presents the structures, symmetries, spin multiplicity, and relative energies with zero point energy (ZPE) correction for the ground state structures and selected low-lying isomers of $AuO(CO_2)_n^{-/+}$ (n = 1–3) clusters. The isomers are arranged in ascending order of energy and labeled as $n\mathrm{A}^{-/+}$, $n\mathrm{B}^{-/+}$, $n\mathrm{C}^{-/+}$ and so on.

3.1.1 $AuO{\cdot}CO_2^-$. The lowest-energy isomer $1A^-$ (C_1 symmetry, singlet state) features a significantly distorted CO_3 fragment. The C–O bond lengths of 1.25 Å, 1.23 Å, and 1.41 Å and the O–C–O bond angles are 132.25°, 107.21° and 120.54°, resulting in an asymmetric structure. In contrast, isomer $1B^-$ (C_s symmetry, triplet state) lies 0.12 eV higher in energy than $1A^-$. $1B^-$ also contains a CO_3 fragment like $1A^-$. The O–C–O

Table 1 Spin multiplicities and corresponding energies of the $AuOCO_2^{-/+}$ clusters

Isomer	Spin multiplicity	Energy (Hartree)
$1A^-$	1	−399.711862
	3	−399.706148
	5	−399.500696
	7	−399.340932
$1A^+$	1	−399.207940
	3	−399.272561
	5	−399.204922
	7	−399.047520

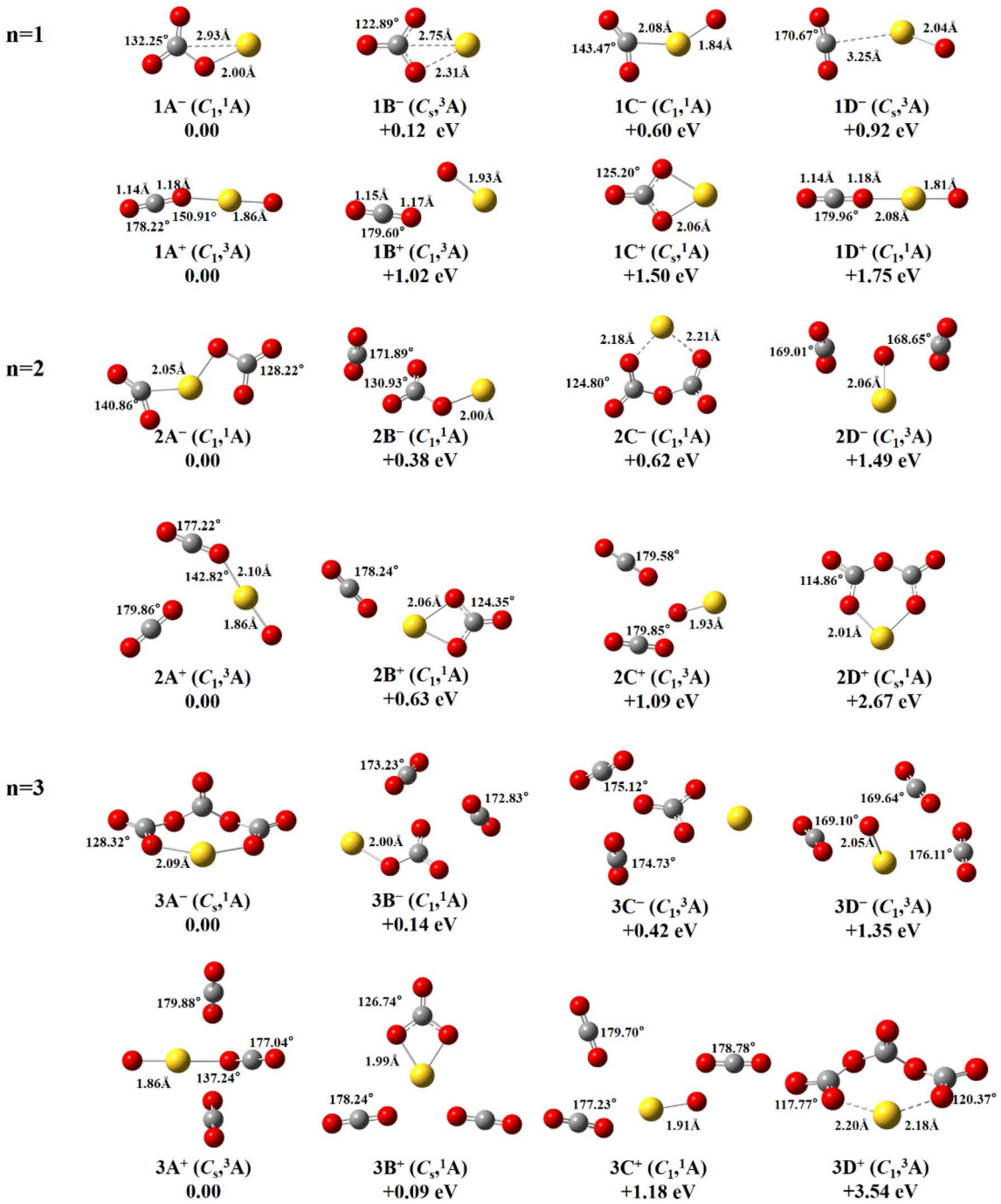

Fig. 1 Optimized structures of the ground state and additional selected low-lying isomers of $AuO(CO_2)_n^{-/+}$ ($n = 1$–3) calculated at the B3LYP-D3/def2-TZVP level of theory (Au, yellow; carbon, gray; oxygen, red). The symmetry, electronic state, the relative energy (eV), bond length (Å) and bond angle (in degrees) are indicated.

angles are 122.89°, 122.90° and 114.21°, and the C–O bond lengths are 1.30 Å, 1.30 Å, and 1.23 Å. The geometric distortion is significantly reduced compared to $1A^-$ but remains clearly different from that of a typical carbonate ion. Isomer $1C^-$ (C_1 symmetry, singlet state) is 0.63 eV higher in energy than $1A^-$. The gold atom coordinates to the carbon of CO_2 in a monodentate fashion, slightly distorting its linear geometry. By contrast, isomer $1D^-$ (C_s symmetry, triplet state), which is 0.92 eV higher in energy than $1A^-$, features weak interaction between Au and CO_2, allowing the CO_2 molecule to retain its nearly linear geometry.

3.1.2 $AuO{\cdot}CO_2^+$. The lowest-energy isomer $1A^+$ (C_1 symmetry, triplet state) adopts a nearly linear CO_2 unit bonded to the AuO moiety *via* a distorted C–O–Au angle of 150.91°. In isomer $1B^+$ (C_1 symmetry, triplet state), which lies 1.02 eV higher in energy than $1A^+$, the gold atom only forms a terminal

Table 2 Thermodynamic stability of the lowest-energy structures of the $AuO(CO_2)_n^{-/+}$ clusters (n = 1–3) at 298 K

Isomer	G(298 K) (au)	ΔG_{ads} (kJ mol^{-1})	G_{bind} (kJ mol^{-1})
$1A^-$	−399.743187	−86.449805	86.449806
$2A^-$	−588.432094	−25.743017	112.192823
$3A^-$	−777.100835	27.202795	84.990028
$1A^+$	−399.305227	−99.944870	99.944870
$2A^+$	−587.986140	−4.754778	104.699649
$3A^+$	−776.663846	3.665196	101.034453

coordination with a single oxygen atom at a bond length of 1.93 Å. Meanwhile, the nearby CO_2 molecule retains its nearly linear geometry. This structure highlights the absence of significant perturbation to the CO_2 molecule, as its geometry is nearly identical to that of a free CO_2 molecule. In isomer $1C^+$ (C_s symmetry, triplet state), the gold atom lies 2.06 Å away from the two oxygen atoms of the distorted CO_3-like unit. This structure resembles $1B^-$, but in $1C^+$ the Au–O distances to the CO_3-like fragment are shorter. $1D^+$ (C_1 symmetry, singlet state) lies 1.75 eV higher in energy than $1A^+$. The structure is characterized by a nearly linear arrangement between the AuO unit and the CO_2 molecule, with both the O–C–O and O–Au–O bond angles approaching 180°.

3.1.3 $AuO(CO_2)_2^-$. For $AuO(CO_2)_2^-$, in the lowest-energy isomer $2A^-$ (C_1 symmetry, singlet state), the gold atom coordinates to two CO_2 molecules. One binds *via* its carbon atom in a monodentate manner, while the other interacts terminally through an oxygen atom. This asymmetric coordination results in a non-linear spatial arrangement of the CO_2 molecules relative to the Au center. In isomer $2B^-$ (C_1 symmetry, singlet state), which lies 0.38 eV above $2A^-$, one CO_2 molecule forms a CO_3-like ligand with the AuO unit, similar to isomer $1A^-$, while the second CO_2 molecule retains a nearly linear geometry with C–O bond lengths of 1.16 Å and an O–C–O bond angle of 171.89°. Positioned 0.62 eV above $2A^-$, isomer $2C^-$ (C_1 symmetry, singlet state) adopts a non-planar, ring-like geometry in which the Au–O distances are 2.18 and 2.21 Å as shown in Fig. 1. In $2D^-$ (C_1 symmetry, triplet state), which is 1.49 eV higher in energy than $2A^-$, both CO_2 molecules retain geometries close to those of free CO_2.

3.1.4 $AuO(CO_2)_2^+$. The lowest-energy isomer $2A^+$ (C_1 symmetry, triplet state) retains the O–Au–CO_2 coordination framework observed in $1A^+$ but exhibits a reduced C–O–Au bond angle. A free CO_2 molecule is present nearby, maintaining a nearly linear geometry with an O–C–O bond angle of 179.86°. Isomer $2B^+$ (C_1 symmetry, singlet state) lies 0.63 eV higher in energy than $2A^+$. Its central structure closely resembles that of $1C^+$, featuring a cyclic CO_3-like unit bonded to the gold atom. The second CO_2 molecule is nearly linear, with an O–C–O bond angle of 178.24°. Isomer $2C^+$ (C_1 symmetry, triplet state) is 1.09 eV higher in energy than $2A^+$. The gold atom coordinates with a single oxygen atom, forming an end-on coordination bond with a length of 1.93 Å. Both CO_2 molecules remain nearly linear, with O–C–O bond angles of 179.58° and 179.85°, respectively. Isomer $2D^+$ (C_s symmetry, singlet state) is 2.67 eV higher in energy than $2A^+$. The structure of $2D^+$ contains a cyclic CO_3-like unit interacting with the gold atom, characterized by an Au–O bond length of 2.01 Å.

3.1.5 $AuO(CO_2)_3^-$. Ground-state isomer $3A^-$ (C_s symmetry, singlet state) forms a eight-membered ring *via* multiple bridging oxygens. This cyclic arrangement contrasts sharply with smaller clusters (n = 1–2), demonstrating size-dependent structural evolution. Isomer $3B^-$ (C_1 symmetry, singlet state), which is 0.14 eV higher in energy than $3A^-$, the core structure resembles that of $1A^-$, while the other two CO_2 units sit apart with O–C–O bond angles of 173.23° and 172.83°, maintaining near-linear geometries. Isomer $3C^-$ (C_1 symmetry, triplet state) is 0.42 eV higher in energy than $3A^-$. The central structure of $3C^-$ resembles that of $1B^-$. And two nearly linear CO_2 molecules are positioned nearby. In isomer $3D^-$ (C_1 symmetry, triplet state) lying 1.35 eV above $3A^-$, all three CO_2 molecules are

Table 3 Activation and bonding indicators for the coordinating CO_2 in the lowest-energy $AuO(CO_2)_n^{-/+}$ structures at 298 K[a]

Isomer	CO_2 id	Δq_{CO_2} (e)	$\delta\theta$ (°)	$\Delta\nu_{as}$ (cm^{-1})	Wiberg Au–O	Wiberg Au–C	Wiberg O_{AuO}–C
$1A^-$	CO_2-a	−0.502	47.75	−1138.84	0.260	0.011	0.000
$2A^-$	CO_2-a	−0.566	51.78	−679.76	0.220	0.013	1.031
	CO_2-b	−0.522	39.14	−510.59	0.324	0.538	0.036
$3A^-$	CO_2-a	−0.206	55.07	−641.63	0.031	0.000	0.000
	CO_2-b	−0.397	51.69	−601.93	0.354	0.000	0.000
	CO_2-c	−0.210	64.27	−579.13	0.036	0.000	1.288
$1A^+$	CO_2-a	+0.122	1.78	+37.91	0.052	0.003	0.000
$2A^+$	CO_2-a	+0.005	2.78	+6.97	0.004	0.000	0.000
	CO_2-b	+0.069	0.14	+29.30	0.052	0.003	0.000
$3A^+$	CO_2-a	+0.005	0.12	+0.01	0.004	0.000	0.000
	CO_2-b	+0.005	0.12	+11.96	0.004	0.000	0.000
	CO_2-c	+0.069	2.96	+24.51	0.052	0.003	0.000

[a] Isomers are the lowest-energy ones ranked by Gibbs free energy at 298 K. Δq_{CO_2} is the NPA charge on each CO_2 unit given by the sum over its C and two O atoms. $\delta\theta$ is 180° minus the O–C–O angle, positive values mean bending. $\Delta\nu_{as}$ is the asymmetric-stretch frequency in the cluster minus the gas-phase value 2410.09 cm^{-1} computed at the same level. Wiberg indices are from NBO. "Au–O" and "Au–C" refer to contacts between Au and the atoms of that CO_2. "O_{AuO}–C" refers to the oxygen in the AuO fragment bonded to the carbon of that CO_2. Labels CO_2-a, CO_2-b, CO_2-c identify different CO_2 units within the same isomer.

positioned around the AuO unit. The O–C–O bond angles of 169.10°, 169.64° and 176.11° show that each CO_2 retains a near-linear geometry.

3.1.6 $AuO(CO_2)_3^+$. The lowest-energy isomer $3A^+$ (C_s symmetry, triplet state) extends the O–Au–CO_2 coordination framework of $1A^+$, with a further reduced C–O–Au angle of 137.24°. Two symmetrically arranged CO_2 ligands retain near-linear geometries, demonstrating charge distribution symmetry. At just 0.09 eV above $3A^+$, isomer $3B^+$ (C_s symmetry, singlet state) contains a central cyclic CO_3-like unit bonded to the gold atom through a 1.99 Å Au–O bond, resembling the coordination in $1C^+$. Two nearly linear CO_2 molecules are symmetrically positioned on either side. Isomer $3C^+$ (C_1 symmetry, singlet state) lies 1.18 eV above $3A^+$ in energy and contains a central gold atom bonded to a single oxygen atom at a bond length of 1.91 Å. Surrounding the central unit are three CO_2 molecules with slightly bent geometries, displaying O–C–O bond angles of 179.70°, 178.78°, and 177.23°. Isomer $3D^+$ (C_1 symmetry, triplet state), lying 3.54 eV above $3A^+$, has an overall structure similar to $3A^-$ but lacks any symmetry and features longer Au–O distances.

Comparison of anionic and cationic clusters reveals that all ground-state anionic clusters with $n = 1$–3 adopt singlet spin multiplicities, whereas the cationic counterparts consistently favor triplet states. In the anionic complexes, the additional electron density promotes the formation of distorted CO_3-like units that strongly coordinate with Au, particularly in the lowest-energy isomers. In contrast, many cationic isomers, especially in higher-lying isomers, exhibit less perturbed, nearly linear CO_2 geometries. Consequently, anionic clusters display more pronounced structural distortions and stronger Au–CO_3 interactions, whereas cationic clusters tend to maintain the linear geometry of CO_2 throughout.

3.2 Activation and bonding indicators

To further elucidate the evolution of structural stability in the $AuO(CO_2)_n^{-/+}$ ($n = 1$–3) clusters, we evaluate the 298 K thermodynamics using two complementary quantities.

The total binding free energy referenced to $AuO^{-/+}$ and n isolated CO_2 molecules is

$$G_{\mathrm{bind}}(n) = [G_{298}(\mathrm{AuO}^{-/+}) + n\, G_{298}(\mathrm{CO_2})] - G_{298}(\mathrm{AuO(CO_2)_n}^{-/+})$$

where a more positive value of G_{bind} indicates stronger stabilization relative to the separated components.

The stepwise adsorption free energy for adding CO_2 is defined as:

$$\Delta G_{\mathrm{ads}}(n) = G_{298}((\mathrm{AuO(CO_2)_n}^{-/+})^{\mathrm{min}}) - G_{298}((\mathrm{AuO(CO_2)_{n-1}}^{-/+})^{\mathrm{min}}) - G_{298}(\mathrm{CO_2})$$

Negative values indicate thermodynamically favorable adsorption.

As summarized in Table 2, for the anions, G_{bind} is 86.45 kJ mol^{-1} at $n = 1$, increases to 112.19 kJ mol^{-1} at $n = 2$, and then decreases to 84.99 kJ mol^{-1} at $n = 3$. The corresponding ΔG_{ads} values are −86.45, −25.74, and +27.20 kJ mol^{-1}, indicating pronounced site saturation that adsorption of the third CO_2 is no longer favorable at 298 K. For the cations, G_{bind} is 99.94 kJ mol^{-1} at $n = 1$, increases to 104.70 kJ mol^{-1} at $n = 2$, and slightly decreases to 101.03 kJ mol^{-1} at $n = 3$. The corresponding ΔG_{ads} values are −99.94, −4.75, and +3.67 kJ mol^{-1}. This gentle evolution is consistent with predominantly electrostatic end-on coordination that keeps CO_2 nearly linear.

To connect these thermodynamic trends with bonding, Table 3 reports activation indicators for the coordinating CO_2 in each lowest-energy structure. The indicators include the fragment charge Δq_{CO_2} from NPA, the deviation from linearity $\delta\theta$, the shift of the asymmetric stretch $\Delta\nu_{\mathrm{as}}$, and Wiberg indices from NBO.

For anions, the indicators substantiate the stability evolution. In $1A^-$ the coordinating CO_2 accepts about 0.50e, deviates by 47.75° from linearity and shows a very large red shift of −1138.84 cm^{-1}, with Au–O Wiberg 0.260 and Au–C essentially zero. In $2A^-$ two motifs coexist. One molecule forms an O–C linkage with the AuO oxygen, characterized by Wiberg O_{AuO}–C 1.031 together with Δq_{CO_2} −0.566e, $\delta\theta$ 51.78° and $\Delta\nu_{\mathrm{as}}$ −679.76 cm^{-1}. The other binds through carbon to Au with Wiberg Au–C 0.538, Δq_{CO_2} −0.522e, $\delta\theta$ 39.14° and $\Delta\nu_{\mathrm{as}}$ −510.59 cm^{-1}, accompanied by moderate Au–O contacts. In $3A^-$ the third CO_2 closes a eight-membered ring *via* multiple bridging oxygens. No Au–C bond is present. The three CO_2 units still accept charge but with smaller magnitude on average, and their asymmetric stretches lie at 1768 to 1831 cm^{-1} giving red shifts of −642 to −579 cm^{-1}. These signatures are weaker than in $1A^-$ and match the onset of site saturation and the positive ΔG_{ads} for the third CO_2 adsorption.

Cationic clusters show weak end-on electrostatic coordination. In $1A^+$ the CO_2 fragment is nearly linear, $\delta\theta$ 1.8°. Δq_{CO_2} + 0.12e and $\Delta\nu_{\mathrm{as}}$ + 38 cm^{-1}. Wiberg Au–O about 0.05 and Au–C essentially zero, which indicates Au–O-dominated contact. In $2A^+$ both CO_2 molecules remain almost linear, $\delta\theta$ up to 2.8°. Δq_{CO_2} values + 0.005 and +0.069e, $\Delta\nu_{\mathrm{as}}$ values + 7 and +29 cm^{-1}. Wiberg Au–O is 0.004 for unit *a* and 0.052 for unit *b*, while Au–C is negligible. In $3A^+$ three nearly linear CO_2 units are retained. $\Delta\nu_{\mathrm{as}}$ spans 0 to 25 cm^{-1}. Only unit *c* shows an appreciable Au–O contact with Wiberg 0.052. These indicators agree with the gentle thermodynamic evolution in Table 2, where ΔG_{ads} changes from −99.94 to −4.75 to +3.67 kJ mol^{-1}, and they explain the persistence of linear CO_2 in the cationic structures.

Taken together, the activation indicators give a consistent picture. In the anionic clusters, the coordinating CO_2 shows pronounced bending and strong red shifts, together with substantial charge uptake and non-negligible Au–O and Au–C Wiberg bond orders. These signatures weaken at $n = 3$, in line with the onset of site saturation. In the cationic clusters, CO_2 remains nearly linear with small or positive $\Delta\nu_{\mathrm{as}}$, minimal charge transfer, and very low Au–O bond orders. Hence, the charge state governs the activation strength, and increasing ligand number attenuates all indicators.

4 Conclusion

This study systematically investigates the geometric and electronic properties of $AuO(CO_2)_n^{-/+}$ (n = 1–3) clusters using density functional theory. The analysis of various isomers reveals that the coordination of the AuO unit with CO_2 induces significant structural distortions and diverse binding motifs, which vary with both the charge state and the cluster size. For the anionic clusters, strong Au coordination results in pronounced distortions of the CO_2 moiety, leading to CO_3-like configurations together with larger charge acceptance on the coordinating CO_2 and enhanced Au–O bonding signatures. Thermodynamic analysis at 298 K, adsorption of the first two ligands is favorable, whereas the third ligand becomes unfavorable, indicating clear site saturation. In contrast, the cationic clusters exhibit more localized charge distributions, with the CO_2 molecules largely retaining their near-linear geometries and experiencing only minor perturbations upon coordination. The thermodynamic evolution with increasing ligand number is gentle for cations, and the third adsorption is slightly unfavorable at 298 K. NPA and NBO analyses corroborate this picture by showing modest charge transfer and low Au–O bond orders for cations, in contrast to stronger charge acceptance and higher Au–O bond orders for anions. Size-dependent structural evolution is evident, with ring-closure motifs emerging at $n = 3$. These findings deepen the mechanistic understanding of CO_2 activation on gold–oxide clusters and provide guidance for designing Au-based motifs in which charge state and site saturation jointly govern adsorption thermodynamics and bonding.

Conflicts of interest

The authors declare that they have no known competing financial interests or personal relationships that could have appeared to influence the work reported in this paper.

Data availability

The data supporting this article have been included as part of the supplementary information (SI). Supplementary information: (i) Table S1 summarizing method sensitivity for $AuO(CO_2)_n^{-/+}$ (n = 1–3); (ii) Table S2 reporting percent differences in Au–O bond lengths and O–C–O angles for each method combination relative to B3LYP/def2-TZVP; and (iii) optimized Cartesian coordinates of the low-lying $AuO(CO_2)_n^{-/+}$ isomers at the B3LYP-D3/def2-TZVP level. See DOI: **https://doi.org/10.1039/d5ra04472c**.

Acknowledgements

This work was supported by the National Natural Science Foundation of China (No. 21976049, 12004094, 12004095, 12304300), the Natural Science Foundation of Hebei Province (No. B2021402006, A2024402007), the Funded By Science and Technology Project of Hebei Education Department (No. BJK2023041), and the Education and Teaching Reform Project of Hebei Province (No. 2023GJJG262).

References

1 P. T. Brown and K. Caldeira, Greater future global warming inferred from Earth's recent energy budget, *Nature*, 2017, **552**, 45–50, DOI: **10.1038/nature24672**.
2 L. Cao, G. Bala, K. Caldeira, R. Nemani and G. Ban-Weiss, Importance of carbon dioxide physiological forcing to future climate change, *Proc. Natl. Acad. Sci. U. S. A.*, 2010, **107**, 9513–9518, DOI: **10.1073/pnas.0913000107**.
3 T. A. Jacobson, J. S. Kler, M. T. Hernke, R. K. Braun, K. C. Meyer and W. E. Funk, Direct human health risks of increased atmospheric carbon dioxide, *Nat Sustainability*, 2019, **2**, 691–701, DOI: **10.1038/s41893-019-0323-1**.
4 M. Aresta, A. Dibenedetto and E. Quaranta, *Reaction Mechanisms in Carbon Dioxide Conversion*, Springer, 2016, pp. 56–57.
5 D. M. D'Alessandro, B. Smit and J. R. Long, Carbon dioxide capture: prospects for new materials, *Angew. Chem., Int. Ed.*, 2010, **49**, 6058–6082, DOI: **10.1002/anie.201000431**.
6 T. M. Gür, Carbon dioxide emissions, capture, storage and utilization: Review of materials, processes and technologies, *Prog. Energy Combust. Sci.*, 2022, **89**, 100965, DOI: **10.1016/j.pecs.2021.100965**.
7 A. M. Appel, J. E. Bercaw, A. B. Bocarsly, H. Dobbek, D. L. DuBois, M. Dupuis, J. G. Ferry, E. Fujita, R. Hille and P. J. Kenis, Frontiers, opportunities, and challenges in biochemical and chemical catalysis of CO_2 fixation, *Chem. Rev.*, 2013, **113**, 6621–6658, DOI: **10.1021/cr300463y**.
8 I. Sullivan, A. Goryachev, I. A. Digdaya, X. Li, H. A. Atwater, D. A. Vermaas and C. Xiang, Coupling electrochemical CO_2 conversion with CO_2 capture, *Nat. Catal.*, 2021, **4**, 952–958, DOI: **10.1038/s41929-021-00699-7**.
9 K. Wei, H. Guan, Q. Luo, J. He and S. Sun, Recent advances in CO_2 capture and reduction, *Nanoscale*, 2022, **14**, 11869–11891, DOI: **10.1039/D2NR02894H**.
10 C. D. Windle and R. N. Perutz, Advances in molecular photocatalytic and electrocatalytic CO_2 reduction, *Coord. Chem. Rev.*, 2012, **256**, 2562–2570, DOI: **10.1016/j.ccr.2012.03.010**.
11 J. J. Fifen and N. Agmon, Structure and spectroscopy of hydrated sodium ions at different temperatures and the cluster stability rules, *J. Chem. Theory Comput.*, 2016, **12**, 1656–1673, DOI: **10.1021/acs.jctc.6b00038**.
12 H. Ke, C. van der Linde and J. M. Lisy, Insights into the Structures of the Gas-Phase Hydrated Cations $M^+(H_2O)_nAr$ (M= Li, Na, K, Rb, and C_s; n = 3–5) Using Infrared Photodissociation Spectroscopy and Thermodynamic Analysis, *J. Phys. Chem. A*, 2015, **119**, 2037–2051, DOI: **10.1021/jp509694h**.
13 A. Malloum, J. J. Fifen and J. Conradie, Structures and spectroscopy of the ammonia eicosamer,$(NH_3)_{n=20}$, *J. Chem. Phys.*, 2018, **149**, 024304, DOI: **10.1063/1.5031790**.
14 A. M. Ricks, A. D. Brathwaite and M. A. Duncan, IR spectroscopy of gas phase $V(CO_2)_n^+$ clusters: solvation-

induced electron transfer and activation of CO_2, *J. Phys. Chem. A*, 2013, **117**, 11490–11498, DOI: 10.1021/jp4089035.

15 M. C. Thompson, J. Ramsay and J. M. Weber, Solvent-driven reductive activation of CO_2 by bismuth: switching from metalloformate complexes to oxalate products, *Angew. Chem., Int. Ed.*, 2016, **55**, 15171–15174, DOI: 10.1002/anie.201607445.

16 H. Wang and N. Agmon, Reinvestigation of the infrared spectrum of the gas-phase protonated water tetramer, *J. Phys. Chem. A*, 2017, **121**, 3056–3070, DOI: 10.1021/acs.jpca.7b01856.

17 R. Wang, G. Liu, S. K. Kim, K. H. Bowen and X. Zhang, Gas-phase CO_2 activation with single electrons, metal atoms, clusters, and molecules, *J. Energy Chem.*, 2021, **63**, 130–137, DOI: 10.1016/j.jechem.2021.09.030.

18 X. Zhang, I. A. Popov, K. A. Lundell, H. Wang, C. Mu, W. Wang, H. Schnöckel, A. I. Boldyrev and K. H. Bowen, Realization of an Al≡Al Triple Bond in the Gas-Phase $Na_3Al_2^-$ Cluster *via* Double Electronic Transmutation, *Angew. Chem., Int. Ed.*, 2018, **57**, 14060–14064, DOI: 10.1002/anie.201806917.

19 Y.-X. Zhao, X.-G. Zhao, Y. Yang, M. Ruan and S.-G. He, Rhodium chemistry: A gas phase cluster study, *J. Chem. Phys.*, 2021, **154**, 180901, DOI: 10.1063/5.0046529.

20 S. Zhou, J. Li, M. Firouzbakht, M. Schlangen and H. Schwarz, Sequential gas-phase activation of carbon dioxide and methane by $[Re(CO)_2]^+$: The sequence of events matters, *J. Am. Chem. Soc.*, 2017, **139**, 6169–6176, DOI: 10.1021/jacs.7b01255.

21 N. Khan, A. Sapi, I. Arora, S. Sagadevan, A. Chandra and S. Garg, Photocatalytic CO_2 reduction using metal and nonmetal doped TiO_2 and its mechanism, *React. Kinet., Mech. Catal.*, 2024, **137**, 629–655, DOI: 10.1007/s11144-024-02601-5.

22 J. Wang, R.-T. Guo, Z.-X. Bi, X. Chen, X. Hu and W.-G. Pan, A review on TiO_{2-x}-based materials for photocatalytic CO_2 reduction, *Nanoscale*, 2022, **14**, 11512–11528, DOI: 10.1039/D2NR02527B.

23 J. Zhao, Y. Wang, Y. Li, X. Yue and C. Wang, Phase-dependent enhancement for CO_2 photocatalytic reduction over CeO_2/TiO_2 catalysts, *Catal. Sci. Technol.*, 2016, **6**, 7967–7975, DOI: 10.1039/C6CY01365A.

24 W. Jiang, H. Loh, B. Q. L. Low, H. Zhu, J. Low, J. Z. X. Heng, K. Y. Tang, Z. Li, X. J. Loh and E. Ye, Role of oxygen vacancy in metal oxides for photocatalytic CO_2 reduction, *Appl. Catal., B*, 2023, **321**, 122079, DOI: 10.1016/j.apcatb.2022.122079.

25 N. H. Khdary, A. S. Alayyar, L. M. Alsarhan, S. Alshihri and M. Mokhtar, Metal oxides as catalyst/supporter for CO_2 capture and conversion, review, *Catalysts*, 2022, **12**, 300, DOI: 10.3390/catal12030300.

26 C. Liu, R.-T. Guo, H.-W. Zhu, H.-F. Cui, M.-Y. Liu and W.-G. Pan, Cu_2O-based catalysts applied for CO_2 electrocatalytic reduction: a review, *J. Mater. Chem. A*, 2024, **12**, 31769–31796, DOI: 10.1039/D4TA06287F.

27 E. I. Brewer, A. E. Green, A. S. Gentleman, P. W. Beardsmore, P. A. Pearcy, G. Meizyte, J. Pickering and S. R. Mackenzie, An infrared study of CO_2 activation by holmium ions, Ho^+ and HoO^+, *Phys. Chem. Chem. Phys.*, 2022, **24**, 22716–22723, DOI: 10.1039/D2CP02862J.

28 Z. Zhao, X. Kong, Q. Yuan, H. Xie, D. Yang, J. Zhao, H. Fan and L. Jiang, Coordination-induced CO_2 fixation into carbonate by metal oxides, *Phys. Chem. Chem. Phys.*, 2018, **20**, 19314–19320, DOI: 10.1039/C8CP02085J.

29 D. Yang, M.-Z. Su, H.-J. Zheng, Z. Zhao, X.-T. Kong, G. Li, H. Xie, W.-Q. Zhang, H.-J. Fan and L. Jiang, Infrared spectroscopy of CO_2 transformation by group III metal monoxide cations, *Chin. J. Chem. Phys.*, 2020, **33**, 160–166, DOI: 10.1063/1674-0068/cjcp1910175.

30 P. Liu, J. Han, Y. Chen, S. Lu, Q. Su, X. Zhou and W. Zhang, Carbon dioxide activation by discandium dioxide cations in the gas phase: a combined investigation of infrared photodissociation spectroscopy and DFT calculations, *Phys. Chem. Chem. Phys.*, 2023, **25**, 32853–32862, DOI: 10.1039/D3CP04995G.

31 P. Liu, J. Han, H. Yu, Y. Chen and X. Zhou, Structural Study of $[Sc_3O_4(CO_2)_n]^+$ (n = 2, 3) Complexes by Infrared Photodissociation Spectroscopy and Density Functional Calculations, *J. Phys. Chem. A*, 2024, **128**, 7158–7166, DOI: 10.1021/acs.jpca.4c04163.

32 N. Walker, G. Grieves, R. Walters and M. Duncan, The metal coordination in $Ni^+(CO_2)_n$ and $NiO_2^+(CO_2)_m$ complexes, *Chem. Phys. Lett.*, 2003, **380**, 230–236, DOI: 10.1016/j.cplett.2003.08.107.

33 X. Kong, R. Shi, C. Wang, H. Zheng, T. Wang, X. Liang, J. Yang, Q. Jing, Y. Liu and H. Han, Interaction between CO_2 and NbO_2^+: Infrared photodissociation spectroscopic and theoretical study, *Chem. Phys.*, 2020, **534**, 110755, DOI: 10.1016/j.chemphys.2020.110755.

34 A. Iskra, A. S. Gentleman, E. M. Cunningham and S. R. Mackenzie, Carbon dioxide binding to metal oxides: Infrared spectroscopy of $NbO_2^+(CO_2)_n$ and $TaO_2^+(CO_2)_n$ complexes, *Int. J. Mass Spectrom.*, 2019, **435**, 93–100, DOI: 10.1016/j.ijms.2018.09.038.

35 J. Han, Y. Yang, B. Qiu, P. Liu, X. Wu, G. Wang, S. Liu and X. Zhou, Infrared photodissociation spectroscopy of mass-selected $[TaO_3(CO_2)_n]^+$ (n = 2–5) complexes in the gas phase, *Phys. Chem. Chem. Phys.*, 2023, **25**, 13198–13208, DOI: 10.1039/D3CP01384G.

36 N. Zimmermann, T. M. Bernhardt, J. M. Bakker, R. N. Barnett, U. Landman and S. M. Lang, Infrared Spectroscopy of Gas-Phase $Mn_xO_y(CO_2)_z^+$ Complexes, *J. Phys. Chem. A*, 2020, **124**, 1561–1566, DOI: 10.1021/acs.jpca.9b11258.

37 P. Mikolaj, B. Z. Yusti, L. Nyulászi, J. M. Bakker, T. Höltzl and S. M. Lang, CO_2 activation by copper oxide clusters: size, composition, and charge state dependence, *Phys. Chem. Chem. Phys.*, 2024, **26**, 24126–24134, DOI: 10.1039/d4cp02651a.

38 E. Hossain, D. W. Rothgeb and C. C. Jarrold, CO_2 reduction by group 6 transition metal suboxide cluster anions, *J. Chem. Phys.*, 2010, **133**, 024305, DOI: 10.1063/1.3455220.

39 L. G. Dodson, M. C. Thompson and J. M. Weber, Interactions of molecular titanium oxides TiO_x (x = 1–3) with carbon

dioxide in cluster anions, *J. Phys. Chem. A*, 2018, **122**, 6909–6917, DOI: 10.1021/acs.jpca.8b06229.

40 R. Pal, L.-M. Wang, Y. Pei, L.-S. Wang and X. C. Zeng, Unraveling the Mechanisms of O_2 Activation by Size-Selected Gold Clusters: Transition from Superoxo to Peroxo Chemisorption, *J. Am. Chem. Soc.*, 2012, **134**, 9438–9445, DOI: 10.1021/ja302902p.

41 N. S. Khetrapal, L.-S. Wang and X. C. Zeng, Determination of CO Adsorption Sites on Gold Clusters Au_n^- (n = 21–25): A Size Region That Bridges the Pyramidal and Core–Shell Structures, *J. Phys. Chem. Lett.*, 2018, **9**, 5430–5439, DOI: 10.1021/acs.jpclett.8b02372.

42 S. M. Lang and T. M. Bernhardt, Cooperative and competitive coadsorption of H_2, O_2, and N_2 on small gold cluster cations, *J. Chem. Phys.*, 2009, **131**, 024310, DOI: 10.1063/1.3168396.

43 P. Pyykkö, Theoretical chemistry of gold. III, *Chem. Soc. Rev.*, 2008, **37**, 1967–1997, DOI: 10.1039/B708613J.

44 H. Häkkinen, Atomic and electronic structure of goldclusters: understanding flakes, cages and superatoms from simple concepts, *Chem. Soc. Rev.*, 2008, **37**, 1847–1859, DOI: 10.1039/B717686B.

45 T. Ishida, T. Murayama, A. Taketoshi and M. Haruta, Importance of Size and Contact Structure of Gold Nanoparticles for the Genesis of Unique Catalytic Processes, *Chem. Rev.*, 2020, **120**, 464–525, DOI: 10.1021/acs.chemrev.9b00551.

46 M. Sankar, N. Dimitratos, P. J. Miedziak, D. J. Morgan and G. J. Hutchings, Role of the Support in Gold-Containing Nanoparticles as Heterogeneous Catalysts, *Chem. Rev.*, 2020, **120**, 3890–3938, DOI: 10.1021/acs.chemrev.9b00662.

47 C. C. Chintawar, A. K. Yadav, A. Kumar, S. P. Sancheti and N. T. Patil, Divergent Gold Catalysis: Unlocking Molecular Diversity through Catalyst Control, *Chem. Rev.*, 2021, **121**, 8478–8558, DOI: 10.1021/acs.chemrev.0c00903.

48 T. Ichino, A. J. Gianola, D. H. Andrews and W. C. Lineberger, Photoelectron Spectroscopy of AuO^- and AuS^-, *J. Phys. Chem. A*, 2004, **108**, 11307–11313, DOI: 10.1021/jp045791w.

49 B. Mehnen, P. S. Żuchowski, D. Kędziera, R. Linguerri and M. Hochlaf, Electronic Structure and Spectroscopy of the AuO^+ Cation, *J. Phys. Chem. A*, 2022, **126**, 8119–8126, DOI: 10.1021/acs.jpca.2c04594.

50 S. M. Lang and T. M. Bernhardt, Gas phase metal cluster model systems for heterogeneous catalysis, *Phys. Chem. Chem. Phys.*, 2012, **14**, 9255–9269, DOI: 10.1039/C2CP40660H.

51 G. E. Johnson, N. M. Reilly, E. C. Tyo and A. W. Castleman Jr., Gas-Phase Reactivity of Gold Oxide Cluster Cations with CO, *J. Phys. Chem. C*, 2008, **112**, 9730–9736, DOI: 10.1021/jp801514d.

52 M. L. Kimble, N. A. Moore, A. W. Castleman Jr., C. Bürgel, R. Mitrić and V. Bonačić-Koutecký, Reactivity of gold oxide cluster anions with CO: experiment and theory, *Eur. Phys. J. D*, 2007, **43**, 205–208, DOI: 10.1140/epjd/e2007-00119-4.

53 T. Lu, *Molclus program, version 1.12*, http://www.keinsci.com/research/molclus.html, accessed April 24, 2024.

54 A. D. Becke, Density-functional exchange-energy approximation with correct asymptotic behavior, *Phys. Rev. A*, 1988, **38**, 3098, DOI: 10.1103/PhysRevA.38.3098.

55 C. Lee, W. Yang and R. G. Parr, Development of the Colle-Salvetti correlation-energy formula into a functional of the electron density, *Phys. Rev. B*, 1988, **37**, 785, DOI: 10.1103/PhysRevB.37.785.

56 S. Grimme, Semiempirical GGA-type density functional constructed with a long-range dispersion correction, *J. Comput. Chem.*, 2006, **27**, 1787–1799, DOI: 10.1002/jcc.20495.

57 F. Weigend and R. Ahlrichs, Balanced basis sets of split valence, triple zeta valence and quadruple zeta valence quality for H to Rn: Design and assessment of accuracy, *Phys. Chem. Chem. Phys.*, 2005, **7**, 3297–3305, DOI: 10.1039/B508541A.

58 D. Andrae, U. Häußermann, M. Dolg, H. Stoll and H. Preuß, Energy-adjusted *ab initio* pseudopotentials for the second and third row transition elements, *Theor. Chem. Acc.*, 1990, **77**, 123–141, DOI: 10.1007/BF01114537.

59 K. P. Kepp, Benchmarking Density Functionals for Chemical Bonds of Gold, *J. Phys. Chem. A*, 2017, **121**, 2022–2034, DOI: 10.1021/acs.jpca.6b12086.

60 L. Huang, W. Liu, J. Hu and X. Xing, Adsorption and Activation of O_2 on Small Gold Oxide Clusters: the Reactivity Dominated by Site-Specific Factors, *J. Phys. Chem. A*, 2022, **126**, 5594–5603, DOI: 10.1021/acs.jpca.2c04438.

61 P. J. Hay and W. R. Wadt, Ab initio effective core potentials for molecular calculations. Potentials for K to Au including the outermost core orbitals, *J. Chem. Phys.*, 1985, **82**, 299–310, DOI: 10.1063/1.448975.

62 P. J. Hay and W. R. Wadt, Ab initio effective core potentials for molecular calculations. Potentials for the transition metal atoms Sc to Hg, *J. Chem. Phys.*, 1985, **82**, 270–283, DOI: 10.1063/1.448799.

63 W. R. Wadt and P. J. Hay, Ab initio effective core potentials for molecular calculations. Potentials for main group elements Na to Bi, *J. Chem. Phys.*, 1985, **82**, 284–298, DOI: 10.1063/1.448800.

64 R. Krishnan, J. S. Binkley, R. Seeger and J. A. Pople, Self-consistent molecular orbital methods. XX. A basis set for correlated wave functions, *J. Chem. Phys.*, 1980, **72**, 650–654, DOI: 10.1063/1.438955.

65 J.-D. Chai and M. Head-Gordon, Long-range corrected hybrid density functionals with damped atom–atom dispersion corrections, *Phys. Chem. Chem. Phys.*, 2008, **10**, 6615–6620, DOI: 10.1039/B810189B.

66 Y. Zhao and D. G. Truhlar, The M06 suite of density functionals for main group thermochemistry, thermochemical kinetics, noncovalent interactions, excited states, and transition elements: Two new functionals and systematic testing of four M06-class functionals and 12 other functionals, *Theor. Chem. Acc.*, 2008, **120**, 215–241, DOI: 10.1007/s00214-007-0310-x.

67 A. E. Reed, L. A. Curtiss and F. Weinhold, Intermolecular interactions from a natural bond orbital, donor–acceptor

viewpoint, *Chem. Rev.*, 1988, **88**, 899–926, DOI: **10.1021/cr00088a005**.

68 M. J. Frisch, G. W. Trucks, H. B. Schlegel, G. E. Scuseria, M. A. Robb, J. R. Cheeseman, G. Scalmani, V. Barone, B. Mennucci, G. A. Petersson, H. Nakatsuji, M. Caricato, X. Li, H. P. Hratchian, A. F. Izmaylov, J. Bloino, G. Zheng, J. L. Sonnenberg, M. Hada, M. Ehara, K. Toyota, R. Fukuda, J. Hasegawa, M. Ishida, T. Nakajima, Y. Honda, O. Kitao, H. Nakai, T. Vreven, J. A. Montgomery, Jr., J. E. Peralta, F. Ogliaro, M. Bearpark, J. J. Heyd, E. Brothers, K. N. Kudin, V. N. Staroverov, R. Kobayashi, J. Normand, K. Raghavachari, A. Rendell, J. C. Burant, S. S. Iyengar, J. Tomasi, M. Cossi, N. Rega, J. M. Millam, M. Klene, J. E. Knox, J. B. Cross, V. Bakken, C. Adamo, J. Jaramillo, R. Gomperts, R. E. Stratmann, O. Yazyev, A. J. Austin, R. Cammi, C. Pomelli, J. W. Ochterski, P. Y. Ayala, K. Morokuma, G. A. Voth, P. Salvador, J. J. Dannenberg, V. G. Zakrzewski, S. Dapprich, A. D. Daniels, O. Farkas, J. B. Foresman, J. V. Ortiz, J. Cioslowski and D. J. Fox, *Gaussian 09, Revision D.01*, Gaussian, Inc., 2009.